International Journal of Mechanical Sciences 138–139 (2018) 476–488

Contents lists available at ScienceDirect

International Journal of Mechanical Sciences

journal homepage: www.elsevier.com/locate/ijmecsci

Material hardening of a high ductility aluminum alloy from a bulge test

Kelin Chen, Martin Scales, Stelios Kyriakides*

Research Center for Mechanics of Solids, Structures & Materials, WRW 110, C0600, The University of Texas at Austin, Austin, TX 78712, United States

ARTICLE INFO

Keywords:
Hydraulic bulge test
Digital image correlation
Anisotropy
Stress–strain response

ABSTRACT

This study employs the hydraulic bulge test in combination with analysis to extract the stress–strain response of an anisotropic Al-6022-T43 sheet metal. Tests are performed in a facility with a 150 mm aperture and the deformation of the bulge is continuously monitored via 3D digital image correlation. The relatively high ductility of this alloy enabled the bulge to deform well past a pressure maximum, reaching a strain of 0.66 at rupture. After the pressure maximum, deformation localized around the apex and the strain profile acquired an increasingly conical shape. Anisotropy is modeled with Barlat's Yld04-3D yield function, calibrated through a set of independent experiments. The measured strains and curvatures at the apex are used in conjunction with membrane equilibrium and Yld04-3D to extract the material stress–strain response. The procedure adopted does not assume an equibiaxial state of stress or strain. A finite element model of the bulge test that includes the draw bead and clamping hardware is used to simulate the experiments. The model accurately reproduces all aspects of the experiment including the strain profile and its localization after the pressure maximum. A parametric study of the problem revealed that the particular anisotropy of the analyzed sheet did not influence the overall behavior of the bulge, but affects the onset of failure in the presence of MK-type thickness imperfections. The amount of material slipping over the draw bead during pressurization, however, is shown to have a more significant impact on the bulge response and the extracted stress–strain response.

1. Introduction

The hydraulic bulge test is the most direct means of measuring the material stress–strain response of sheet metal to strains far larger than what is possible in other tests. It typically involves a circular disc clamped around its perimeter that is inflated by hydraulic pressure to form a bulge. The nearly-equibiaxial stress state at the apex, and the continuous reduction in local radius as the bulge height increases, delay wall thinning and the limit pressure instability. The strain and radius at the apex of the bulge, used in conjunction with a flow rule and the membrane equilibrium equation, enable extraction of the stress–strain response. Measurements of the strain and radius were initially performed manually (e.g., [1–3]) making the test cumbersome and limiting its wider use. The introduction of a spherometer (e.g., [4]) and similar devices (e.g., [5,6]) simplified the acquisition of these measurements and made the test more accessible.

The more recent development of full-field optical methods like digital image correlation has expanded the measurements that can be made and further simplified their extraction, providing new impetus to the use of the bulge test (e.g., [7–10]). The ability to measure the exact shape and strains at the apex coupled with numerical modeling of the test has enabled analysis of anisotropy, through thickness effects, strain rate, and failure ([10–14]).

Analytical considerations of the bulge test have an equally long history, beginning with Gleyzal [15] and Hill's [16] extension of an approximated but insightful analysis of the problem. Chakrabarty and Alexander [17] pushed Hill's analysis forward by considering the effects of material hardening, while others investigated factors such as thickness effects, elliptical apertures, etc. (see [3,18–20] among others).

This paper presents a combined experimental and analytical procedure for extracting the stress–strain response of an anisotropic sheet metal using the bulge test. The procedure follows the general guidelines of Chen et al. [12]. Differences in the material properties and more uniform clamping provide a simpler setting for the analysis and bring to fore new insights about the bulge test. The material analyzed is Al-6022-T43, an alloy aimed at automotive sheet metal forming [21]. In this heat treatment it has a rather low initial yield stress, but exhibits significant hardening and greater ductility than other aluminum alloys (see basic properties in Table 1 and nominal stress–strain response in Fig. A1). The material can be further hardened following forming by heat treatment such as that experienced during the paint bake cycle. Experiments on 1.20 mm thick sheets are conducted in our 150 mm (6 in) aperture bulge testing facility, using stereo DIC to continuously monitor the evolution of deformation.

* Corresponding author.
E-mail address: skk@mail.utexas.edu (S. Kyriakides).

https://doi.org/10.1016/j.ijmecsci.2018.02.002
Received 21 December 2017; Received in revised form 31 January 2018; Accepted 1 February 2018
Available online 5 February 2018
0020-7403/

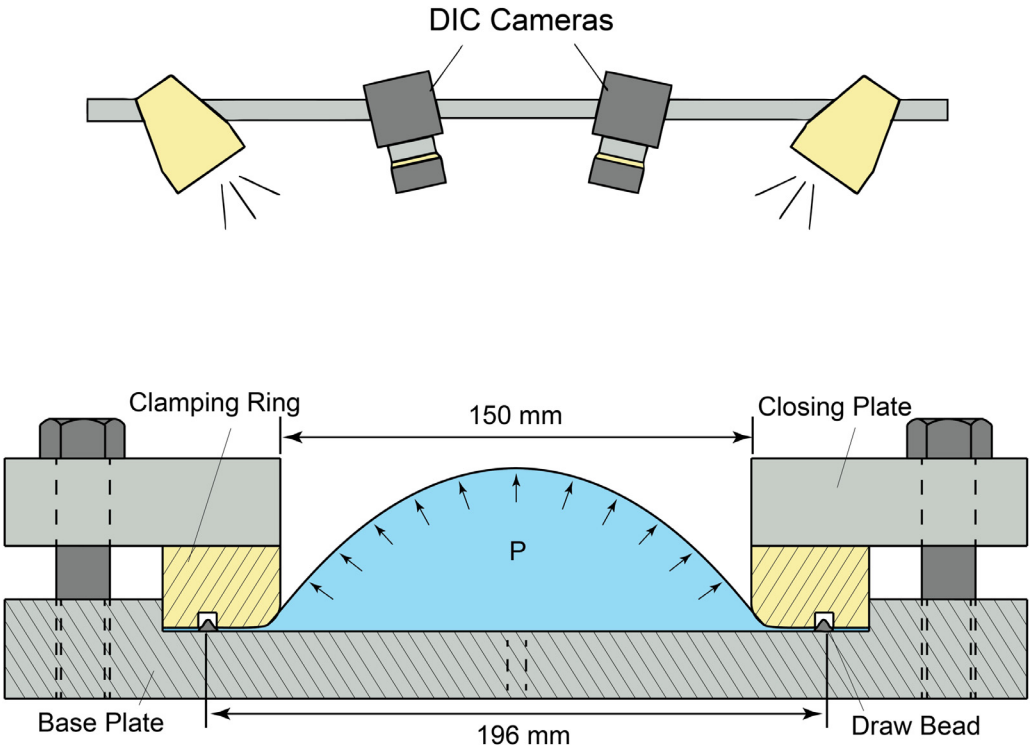

Fig. 1. Cross section and selected dimensions of the bulge test facility.

Table 1
The rolling direction material parameters of Al-6022-T43 sheet analyzed.

t_o in (mm)	E Msi (GPa)	ν	$\sigma_{ox'}$ ksi (MPa)	$\sigma_{ux'}$ ksi (MPa)	$\varepsilon_{ux'}$
0.0474 (1.20)	10.2 (70.3)	0.32	22.5 (155)	37.9 (262)	0.227

The anisotropy of the sheet is established using an independent set of experiments, which are used to calibrate the Yld04-3D non-quadratic yield function of Barlat et al. [22]. A membrane stress state is assumed to exist at the apex but neither an equibiaxial state of stress or strain is assumed. Instead, the stress–strain response is extracted incrementally using the measured strains and radii of curvature in the two principal directions together with the constitutive and equilibrium equations.

The extracted stress–strain response and the Yld04-3D constitutive model are then implemented in a finite element model of the bulge test and used to numerically simulate the bulge experiment and to assess the onset of failure. Comparison of the measured and calculated response is used to evaluate the whole process. In the way of evaluating commonly used extrapolations of the uniaxial response, three such extrapolations are compared with the one extracted from the bulge test.

2. Bulge experiments and results

The bulge experiments are performed using the custom-built hydraulic bulge testing facility shown schematically in Fig. 1. The design was influenced by the Kuwabara facility in [23]. The base plate has a 229 mm (9 in = $2R_o$) diameter recess that holds the sheet metal test specimen. It is locked in place by a clamping ring that presses the specimen against a draw bead machined into the base plate at a diameter of 196 mm (7.72 in = $2R_1$). The contact surface of the clamping ring has a radius of 8.0 mm (0.315 in). Clamping is achieved by tightening eight bolts that engage a closing plate at the top and thread into the base plate as shown in Fig. 1. The arrangement leaves a 150 mm (6.0 in = $2R$) aperture in which the bulge develops (in accordance with ISO2014 [9] guidelines). The system is pressurized with light oil using a closed-loop servo-hydraulic pressurization system operated under volume control (see Fig. 2 of [12]).

DIC is used to continuously monitor the bulge throughout the test. The system consists of two 5 MP digital cameras equipped with 50 mm lenses set at an f/16 aperture. The setup provides a 70 mm (2.76 in) depth of field and a 80 × 70 mm (3.15 × 2.76) measuring area. Images were acquired at 2 s intervals initially but faster as failure approached. Deformations were calculated from the recorded images using GOM ARAMIS v6.3 [24]. A facet size of 40 × 40 pixels (~1.19 × 1.19 mm–0.047 × 0.047 in) and a facet spacing of 10 pixels (0.30 mm–0.012 in) provide a good balance between resolution and accuracy at the apex of the bulge.

Fig. 2 summarizes the measured results from one of the bulge experiments on Al-6022-T43 discs (experiment BT1). In Fig. 2a the pressure, P, is plotted against the bulge height, h, normalized by the aperture radius, R. The pressure rises nearly linearly with h up to about 55 bar (800 psi) when the rate of increase slows down. The decrease in the rate at which pressure increases continues until a pressure maximum develops at 64.0 bar (928 psi), which is indicated on the response by a caret "^". Deformation continues beyond this critical state with the pressure decreasing until it ruptures at 63.79 bar (925 psi).

The radii of curvature in the rolling ($\rho_{x'}/R$) and transverse direction ($\rho_{y'}/R$) at the apex are plotted against the normalized height in Fig. 2b. Each is determined from the DIC data by fitting a circle to the points that are located within 15.2 mm (0.6 in) of the apex (size chosen to minimize errors–see [10]). The two radii drop significantly with h, reaching a value close to R just before rupture; notably they remain approximately equal to each other throughout the experiment.

The measured logarithmic strains at the apex in the rolling ($e_{x'}$) and transverse ($e_{y'}$) directions are plotted against the pressure in Fig. 2c (averaged over a distance of 7.6 mm (0.3 in) from the apex). The two strains differ throughout the test, presumably because of the anisotropy in the sheet. The results indicate that the rolling and transverse directions are the principal directions. The through thickness strain at the apex, $e_{z'}$,

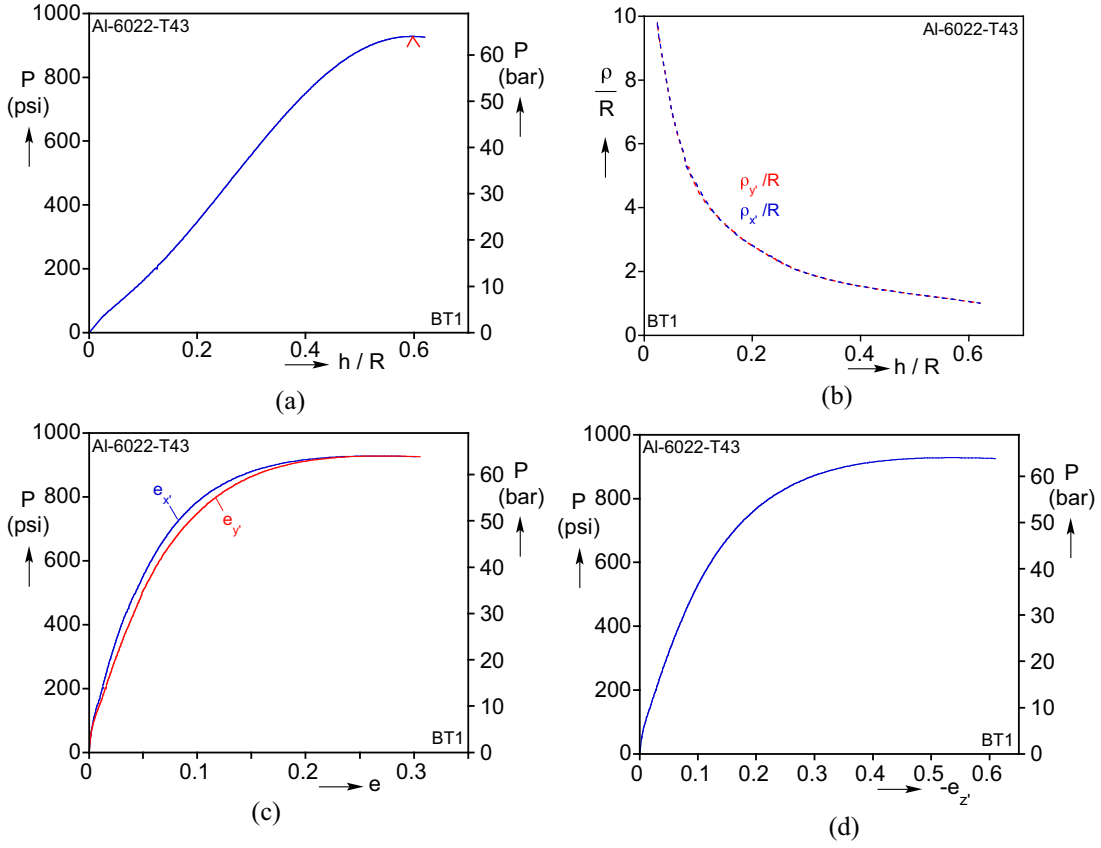

Fig. 2. Summary of experimental results from a bulge test (BT1): (a) Pressure versus normalized apex height. (b) Normalized radii of curvature at the apex in the rolling (x') and transverse (y') directions. (c) Pressure versus measured logarithmic strains at the apex in the x' and y' directions. (d) Pressure versus approximate through-thickness logarithmic strain at the apex.

is then directly obtained from incompressibility and is plotted against pressure in Fig. 2d. The strain rate at the apex was about $4\times10^{-4}\,s^{-1}$ at lower pressures and increased with time to $30\times10^{-4}\,s^{-1}$ at the end of the test.

A second bulge test (BT2) was performed on material from the same sheet and exhibited essentially the same behavior quantitatively and qualitatively. Images in this experiment were acquired at the much faster rate of 5/s from just before the pressure maximum until failure, providing for a much more detailed analysis of the evolution of deformation. Fig. 3a shows the recorded pressure plotted against the bulge height. The response is nearly identical to that of BT1 in Fig. 2a, but extends slightly further past the limit pressure. The pressure reached a maximum value of 64.26 bar (932.8 psi) and dropped to 63.81 bar (925.2 psi) at failure.

The evolution of the bulge profile along a meridian oriented along the diagonal of the rectangular area monitored by DIC is plotted in Fig. 3b with r being the radial distance from the center of the disc. The profiles correspond to the pressure and bulge height marked with numbered bullets in Fig. 3a. Profile ⑦, drawn in red color, corresponds to the pressure maximum. The curvature of the partial bulge profiles shown increases continuously but less so at higher pressures. The shape of the profiles is nearly circular after the pressure maximum also. Fig. 3c shows the von Mises equivalent strain (e_e) along the ten profiles. In the first three stages the strain gradually increases but each profile remains rather flat. The strain at the apex becomes increasingly greater in profiles ④-⑦ while the strain further from the apex grows far less rapidly. In profile ⑦ at the pressure maximum, the strain at the apex is 0.53 and drops down to 0.29 at $r \approx -0.64R$. Following the pressure maximum, the strain profiles take on a more conical shape with higher deformation becoming increasingly concentrated around the apex and decreasing nearly linearly outward from there. This of course implies that wall thinning accelerated after the pressure maximum at the apex. The highest strain recorded just before failure is 0.66. It is worth pointing out that discreet local thickness measurements performed in the neighborhood of such ruptures, were found to be in good agreement with the values evaluated from the DIC measured surface strains using incompressibility. Interestingly, Brown and Sachs [1] reported similar conical strain profiles in OFHC copper sheets in their classic work on the bulge test. They measured the strains manually from the deformation of a photogrid. Similar profiles were also reported recently in [10] and [13], both using DIC to monitor the strains in bulge experiments on DC06 and DX54 steels respectively.

Fig. 4 shows one of the tested specimens (BT2) removed from the testing facility. In these experiments, failure consistently initiated at the apex and developed into a crack that initially was nearly normal to the rolling direction of the sheet. Driven by the energy stored in the relatively compliant test system, the crack propagated dynamically. In this case the crack propagated along an essentially linear path normal to the rolling direction. In the last image recorded just before rupture, the specimen remained intact with no observed signs of localization. It is worth pointing out that the clamped outer rim of the specimen exhibits no wrinkling, indicating that slipping at the draw bead was minimal. Furthermore, the uniform width of the rim outside the draw bead suggests that asymmetric slipping was also minimal, unlike what was experienced in the Al-2024-T3 specimens reported [12] (e.g., see specimen in Fig. C1).

2.1. Data analysis

Assuming that a membrane state of stress exists at the apex, the stresses in the rolling and transverse direction ($\tau_{x'},\tau_{y'}$) are related to the pressure and the geometry of the bulge through the equilibrium

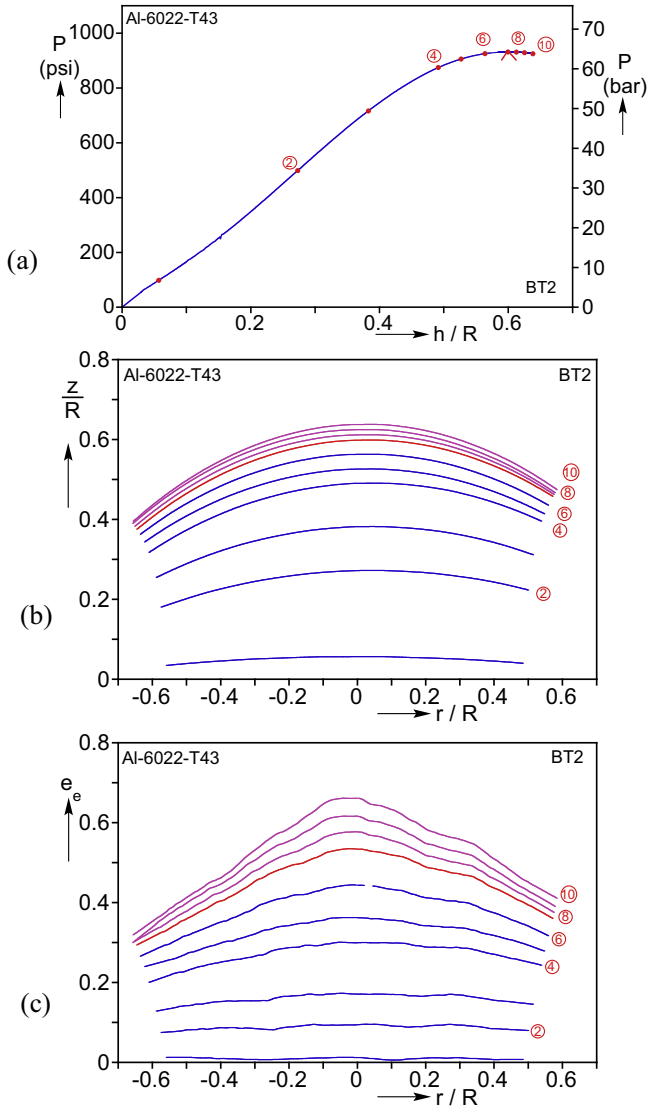

Fig. 3. Evolution of bulge deformation in experiment BT2. (a) Pressure versus apex height response, (b) deformed surface profiles across the apex, and (c) corresponding equivalent strain profiles (profiles correspond to numbered bullets on the response in (a)).

equation

$$\frac{\tau_{x'}}{\rho_{x'}} + \frac{\tau_{y'}}{\rho_{y'}} = \frac{P}{t} \tag{1}$$

where t is the current wall thickness. Note that the stresses and radii in the two directions can be different because of anisotropy [20]. Following [12] the following stress ratio is formed,

$$\tau_{y'} = \alpha \tau_{x'} \tag{2a}$$

so that from Eq. (1)

$$\tau_{x'} = \frac{P}{t}\left(\frac{1}{\rho_{x'}} + \frac{\alpha}{\rho_{y'}}\right)^{-1} \text{ and } \tau_{y'} = \frac{\alpha P}{t}\left(\frac{1}{\rho_{x'}} + \frac{\alpha}{\rho_{y'}}\right)^{-1}. \tag{2b}$$

It's worth noting Eqs. (2) are simpler than in [12] because $\{e_{x'}, e_{y'}\}$ are the principal strains. Using the calibrated anisotropic yield function, Φ, in the flow rule the instantaneous strain ratio is related to the stress ratio through

$$\frac{de^p_{y'}}{de^p_{x'}} = \frac{\partial \Phi / \partial \tau_{y'}}{\partial \Phi / \partial \tau_{x'}} = r(\alpha) \tag{3}$$

Fig. 4. Experiment BT2 specimen after the test.

(in the calibration scheme adopted Φ defined in Eq. (9) is evaluated iteratively as described in Section 3).

The instantaneous strain ratio is evaluated from the measured strains by assuming the elastic deformations to be negligibly small. Eq. (3) is solved numerically for α for each strain increment and the corresponding stresses follow from (2). The yield function is then used to evaluate the equivalent stress, τ_e, and the equivalent plastic strain increment is calculated as follows:

$$de^p_e = \frac{\tau_{x'} de^p_{x'} + \tau_{y'} de^p_{y'}}{\tau_e}. \tag{4}$$

In this fashion the equivalent plastic stress–strain response of the material is produced incrementally.

The measured data are also used to generate stress–strain responses for the isotropic yield functions of von Mises and Hosford [25] with an exponent of 8. For these purposes the apex of the bulge is assumed to form a spherical cap of radius ρ, which is calculated from the DIC data by fitting a sphere to the coordinates of all points within a 0.6-in (15.2 mm) radius of the apex. Thus the stresses are given by

$$\tau_1 = \tau_2 = \frac{P\rho}{2t} = \tau_e \tag{5a}$$

and the strains are averaged so that

$$de_1 = de_2 = (de_{x'} + de_{y'})/2 \text{ and } de_e = 2de_1. \tag{5b}$$

3. Constitutive models and calibration

As in our past works dealing with the deformation, localization and failure of thin-walled aluminum alloy structures, the anisotropic Yld04-3D model of Barlat et al. [22] is adopted in the present analysis on Al-6022-T43 (see [12,26,27]; [28–31] who used Yld2000-2D for shell element models; and [32] who used an extension of the last model in a 3D setting, Yld2000-3D). Hosford's isotropic non-quadratic yield function expressed in terms of the principal deviatoric stresses is given by:

$$|s_1 - s_2|^k + |s_2 - s_3|^k + |s_3 - s_1|^k = 2\sigma_o^k. \tag{6}$$

Barlat et al. [22] introduce anisotropy through two linear transformations to construct the tensors $\boldsymbol{S'}$ and $\boldsymbol{S''}$ from the Cauchy stress as follows:

$$\boldsymbol{S'} = \boldsymbol{C's} = \boldsymbol{C'T\sigma} = \boldsymbol{L'\sigma} \text{ and } \boldsymbol{S''} = \boldsymbol{C''s} = \boldsymbol{C''T\sigma} = \boldsymbol{L''\sigma} \tag{7}$$

where $\boldsymbol{C'}$, $\boldsymbol{C''}$, $\boldsymbol{T}$, $\boldsymbol{L'}$, $\boldsymbol{L''}$ are transformation tensors. $\boldsymbol{T}$ transforms $\boldsymbol{\sigma}$ to $\boldsymbol{s}$ and $\boldsymbol{C'}$, $\boldsymbol{C''}$ contain the following anisotropy parameters.

$$\boldsymbol{C'} = \begin{bmatrix} 0 & -c'_{12} & -c'_{13} & 0 & 0 & 0 \\ -c'_{21} & 0 & -c'_{23} & 0 & 0 & 0 \\ -c'_{31} & -c'_{32} & 0 & 0 & 0 & 0 \\ 0 & 0 & 0 & c'_{44} & 0 & 0 \\ 0 & 0 & 0 & 0 & c'_{55} & 0 \\ 0 & 0 & 0 & 0 & 0 & c'_{66} \end{bmatrix},$$

$$\boldsymbol{C''} = \begin{bmatrix} 0 & -c''_{12} & -c''_{13} & 0 & 0 & 0 \\ -c''_{21} & 0 & -c''_{23} & 0 & 0 & 0 \\ -c''_{31} & -c''_{32} & 0 & 0 & 0 & 0 \\ 0 & 0 & 0 & c''_{44} & 0 & 0 \\ 0 & 0 & 0 & 0 & c''_{55} & 0 \\ 0 & 0 & 0 & 0 & 0 & c''_{66} \end{bmatrix}. \tag{8}$$

The yield function in terms of the principal values of $\boldsymbol{S'}$ and $\boldsymbol{S''}$ then becomes:

$$\begin{aligned} \Phi = \Big[\Big(& \left|S'_1 - S''_1\right|^k + \left|S'_1 - S''_2\right|^k + \left|S'_1 - S''_3\right|^k \\ & + \left|S'_2 - S''_1\right|^k + \left|S'_2 - S''_2\right|^k + \left|S'_2 - S''_3\right|^k \\ & + \left|S'_3 - S''_1\right|^k + \left|S'_3 - S''_2\right|^k + \left|S'_3 - S''_3\right|^k \Big) \Big/ 4 \Big]^{1/k} \end{aligned} \tag{9}$$

where again k is assigned the value 8. Details about the derivations and the derivatives of the yield function with respect to the stress components can be found in [22] and [33] (model implemented in a subroutine by Yoon [34]).

The anisotropy parameters are established from a set of independent tests on specimens extracted from the same sheet that the bulge test discs originated from. The calibration involves the following three sets of experiments:

(a) Seven uniaxial tests on specimens oriented at 15° intervals between the rolling and transverse directions. The measured true stress-logarithmic strain responses are shown truncated in Fig. A2a and the corresponding axial–transverse strain responses in Fig. A2b.
(b) Three plane strain tests on specimens with the geometry shown in Fig. A3a oriented along the rolling, transverse, and 45° directions. The estimated axial stress-measured logarithmic axial strain responses, $\tau_x - e_x$, are plotted in Fig. A3b.
(c) The bulge test itself, from which the strain ratio and the extracted stresses at the apex are used. Fig. A4 plots the measured strains $\{e_{y'}(P), e_{x'}(P)\}$ against each other. In the regime of interest to the calibration they are linearly related with a ratio of 1.18.

More details on the calibration procedure can be found in [12,22,27].

For each of the 10 experiments under (a) and (b), we calculate the stress state and strain ratios in the material coordinate system at a chosen value of plastic work ($W^p = 10.3$ MPa–1500 psi). The yield function (9) is used to calculate the equivalent stresses in terms of the unknown constants $\{c'_{ij}, c''_{ij}\}$. Error functions are generated for each experiment, comparing the calculated equivalent stresses to the rolling-direction uniaxial flow stress ($\tau_{x'0}$) at the same value of plastic work. The stress state of each experiment is used in the flow rule to calculate the strain ratios again in terms of the constants $\{c'_{ij}, c''_{ij}\}$. Additional error functions are formed that compare these strain ratios to the values measured in the experiments at the chosen value of plastic work (see Appendix A in [12] for details; a similar set of experiments, without the bulge test stresses, was used by [35] to calibrate the Yld2000-2D model for the same alloy with a T4 heat treatment.)

Data from the bulge test are used to inform the yield surface in the neighborhood of the equibiaxial stress state. The experiment provided the strains and radii of curvature at the apex, but the stresses must be established through an iterative process that involves recalculating $\{c'_{ij}, c''_{ij}\}$ in each iteration. Initially, the stress state is assumed to be equibiaxial ($\tau_e = P\rho/2t$), the strain ratio is set at 1.0, and these values are used to generate error functions similar to those described above.

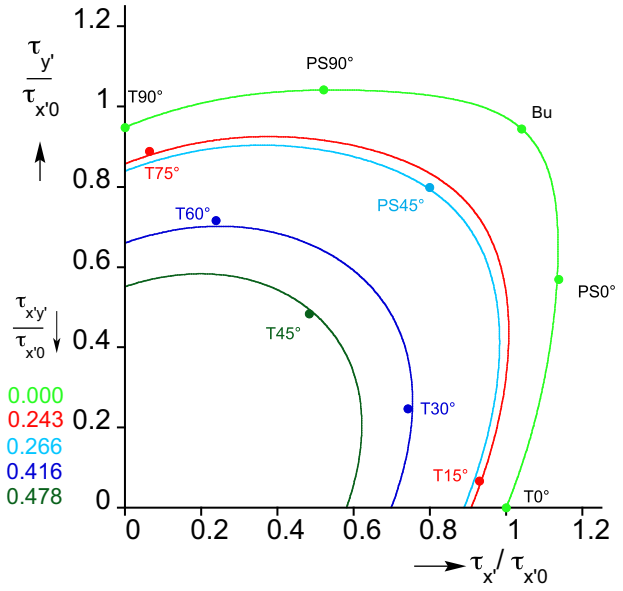

Fig. 5. Work contours of the calibrated Yld04-3D constitutive model in the rolling-transverse stress space at varying levels of shear. Experimental data used in calibration are included with solid bullets (T = tension, PS = plane strain, Bu = bulge test).

The following weighted sum of the 22 error functions is then generated

$$\mathcal{E}(c'_{ij}, c''_{ij}) = \sum_m \omega_m \left(\frac{\tau_{e\phi}}{\tau_{x'0}} - 1 \right)_m^2 + \sum_n \omega_n \left(\frac{R_\phi}{R_{ex}} - 1 \right)_n^2. \tag{10}$$

Here the first series represents errors from the m flow stresses, the second the errors from the n strain ratios, and $\{\omega_m, \omega_n\}$ are weight functions that represent the confidence level assigned to each particular experiment. $\mathcal{E}(c'_{ij}, c''_{ij})$ is minimized using the *NMinimize* routine of Mathematica to provide a first estimate of the constants $\{c'_{ij}, c''_{ij}\}$.

The stress history at the bulge apex is now recalculated using the newly calibrated yield function and flow rule in Eqs. (1)–(3). The new stress state and strain ratio of the bulge apex at the chosen value of plastic work are used to update the corresponding error functions. The minimization of the global error function (10) is then repeated to generate a new set of $\{c'_{ij}, c''_{ij}\}$. The bulge apex variables are again recalculated and compared to the results of the previous iteration cycle; when the two sets of results agree the calibration process is considered to have converged.

The values of the anisotropy constants determined from this calibration process are listed in Table 2. In the absence of through thickness shear measurements the constants $\{c'_{44}, c'_{55}, c''_{44}, c''_{55}\}$ were set at 1.0. It is worth pointing out that the estimated values of the constants are influenced to some degree by the weights $\{\omega_m, \omega_n\}$ used in (10) and by the initial guess of the bulge apex stresses.

In general the results of such calibration processes are not unique. To further evaluate the present solution the calibrated yield function and some of the corresponding experimental points are compared in Fig. 5 (T = tension, PS = plane strain, Bu = bulge test). Plotted are the work contours in the $\tau_{x'}$-$\tau_{y'}$ plane both normalized by the measured stress in the rolling direction, $\tau_{x'0}$, at $W^p = 10.3$ MPa (1500 psi) for different values of normalized shear stress ($\tau_{x'y'}/\tau_{x'0}$). The comparison of experimental data and the calibrated work contour is quite favorable. Fig. 6 shows a similar comparison of the work contours corresponding to the isotopic version of the yield function in Eq. (6) (H8) with the same

Table 2
Yld04-3D anisotropy parameters for Al-6022-T43.

c'_{12}	c'_{13}	c'_{21}	c'_{23}	c'_{31}	c'_{32}	c'_{44}	c'_{55}	c'_{66}
1.0140	0.5047	0.7951	0.6976	0.5089	0.4509	1.0	1.0	1.1980
c''_{12}	c''_{13}	c''_{21}	c''_{23}	c''_{31}	c''_{32}	c''_{44}	c''_{55}	c''_{66}
1.0217	1.4496	0.8892	1.1418	1.3136	1.5447	1.0	1.0	0.5664

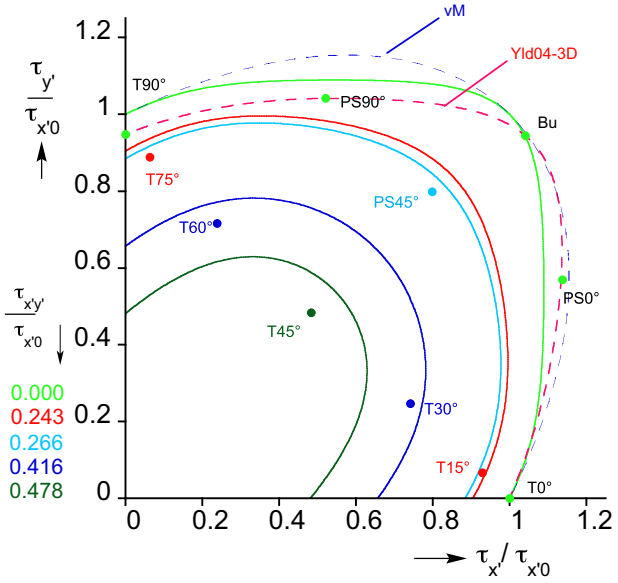

Fig. 6. Work contours of the isotropic H8 model in the rolling-transverse stress space at varying levels of shear, with the same experimental data as in Fig. 5.

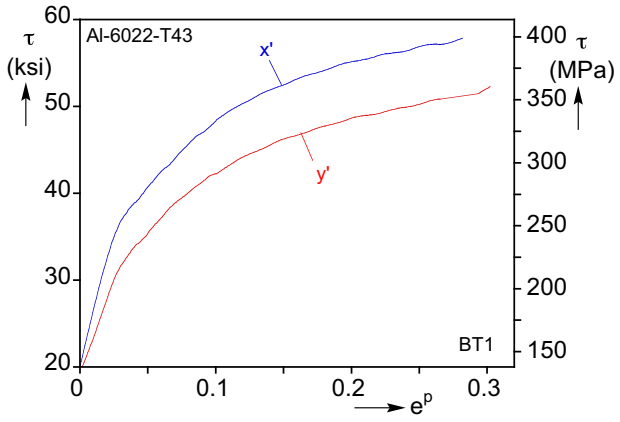

Fig. 7. Calculated stress-plastic strain responses in the rolling and transverse directions.

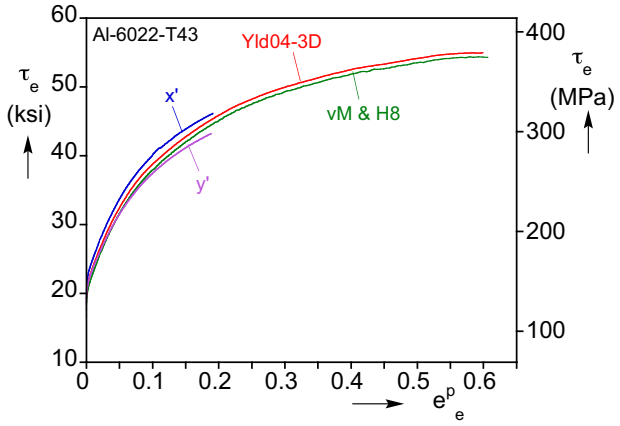

Fig. 8. Extracted equivalent stress-plastic strain response using the calibrated Yld04-3D anisotropic yield function, and the isotropic vM and H8 functions. Included for reference are stress-plastic strain responses measured in uniaxial tension tests in the rolling and transverse directions.

experimental data. Significant differences between the calculated work contours and all but two experimental points are observed, which must be the result of the anisotropy in the sheets. The results in Figs. 5 and 6 provide support for the validity of the results of the anisotropy calibration procedure.

3.1. Extraction of the stress–strain response from the bulge test

The calibrated yield function is now used to extract the material stress–strain response from the experimental results from the apex of the bulge test reported in Section 2. Eq. (3) is solved numerically for the stress ratio α for measured values of the strain ratio. α is then used in Eq. (2) to calculate the two stresses $\{\tau_{x'},\tau_{y'}\}$. They are plotted against the measured logarithmic plastic strains in the rolling and transverse directions in Fig. 7. In contrast to the corresponding results for Al-2024-T3 (F10b in [12]), the responses are noticeably different, which is a manifestation of the more significant anisotropy in the Al-6022-T43 sheet metal.

The calculated stresses are now used in the calibrated yield function (9) to establish the equivalent stress, τ_e. The corresponding plastic equivalent strain, e^p_e, is subsequently evaluated using Eq. (4). The result of this process is the stress-plastic strain response plotted in Fig. 8 and identified by Yld04-3D. The response has a yield stress of about 138 MPa (20 ksi) and rises to 379 MPa (55 ksi) at the terminal strain of just over 0.60. Included in the figure are the measured uniaxial responses in the rolling, x', and transverse, y', directions. They exhibit a similar hardening to the rolling direction, tracing a slightly higher stress trajectory, and the transverse direction slightly lower. Both terminate at strains of about 0.20, which demonstrates the advantages of using the bulge test to establish the material response of sheet metal.

We include in Fig. 8 the stress-plastic strain response extracted from the bulge test results using the Hosford yield function (H8) (i.e., by neglecting anisotropy and assuming the apex to be a spherical cap of radius ρ as in Eqs. (5); under these assumptions the von Mises yield function (vM) produces the same response). The response follows a similar trajectory, tracing slightly lower stress levels than the Yld04-3D results. This can be explained by comparing the work contours corresponding to $\tau_{x'y'}=0$ of the three models in Fig. 6. In the neighborhood of equibiaxial stress the three contours are very similar which leads to similar equivalent stress for the extracted response. The implications of this similarity on the numerical simulation of the bulge test will be discussed in Section 4.

In the sheet metal manufacturing practice the bulge test is often avoided. The alternative method of extracting the material response from the necked regime of a uniaxial test using inverse analysis (e.g., [27]) is even more challenging and less common. Instead, the stress–strain response from a uniaxial test is often extrapolated using one of the traditional fits such as that of Swift [36] or Voce [37]. The first, $\tau = k(A+e^p)^N$, assumes power law hardening and in the second, $\tau = a+(\tau_o - a)exp(-be^p)$, the hardening decays exponentially at higher

Table 3
Parameters for the Swift and Voce fits of the uniaxial stress–strain response.

Swift			Voce		
k MPa (ksi)	A	N	a MPa (ksi)	τ_o MPa (ksi)	b
483.4 (70.09)	0.0051	0.2512	347.3 (50.36)	163.0 (23.78)	9.4587

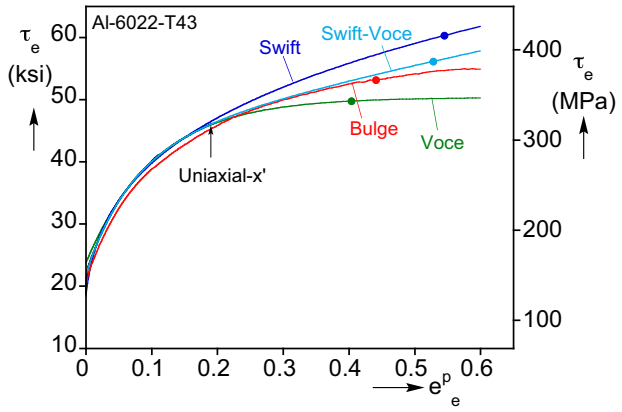

Fig. 9. Comparison of the equivalent stress-plastic strain response evaluated from our bulge test, and extrapolations of the uniaxial tension response of Swift and Voce and a combination of the two. The uniaxial response in the rolling direction is included for reference. The solid bullets identify the values of equivalent stress and strain at the pressure maximum predicted by Hill's approximate analysis of the bulge (see Appendix B).

strains. In the way of evaluating their performance against the stress–strain response extracted from the bulge test, the two expressions are fitted to the uniaxial response measured in the rolling direction.

The fit constants are listed in Table 3 and the resultant stress-plastic strain responses, extrapolated to a strain of about 0.60, are plotted in Fig. 9 together with the response extracted from the bulge test. Both fit the uniaxial and bulge responses well up to a plastic strain of about 0.20. But at higher strains the Swift extrapolation significantly overestimates the bulge response whereas the Voce extrapolation saturates early and considerably underestimates the hardening (see also [13,38]). Differences of this extent in plastic modulus can lead to significant errors in the prediction of instabilities such as localization and wrinkling that are common in sheet metal forming. More recently, some authors have opted to fit the uniaxial stress–strain response using a combination of Swift and Voce (e.g., [39]). Included in Fig. 9 is such an extrapolated fit. As expected, it is much closer to the response extracted from the bulge test than the two individual fits. It follows the measured response up to a strain of 35% and overestimates the tangent modulus at higher strains.

4. Finite element modeling

A finite element model of the bulge test is developed in ABAQUS and the experiment reported in Section 2 is simulated using the calibrated Yld04-3D yield function and the extracted stress–strain response. The model incorporates the precise geometry of the experimental set up including the draw bead. Fig. 10a shows the finite element mesh of only one quarter of the model for clarity. The disc rests on the draw bead of the circular base located at $R_1 = 98$ mm (3.86 in) as shown in Fig. 10b. This figure includes the clamping ring which has an inner radius $R = 76.2$ mm (3.00 in) and a rounded profile radius on its inner surface of 8.0 mm (0.315 in). Chen et al. [12] demonstrated that even small amounts of slipping at the draw bead can influence the results of the bulge test. Accordingly in order to examine this effect in the present study the model includes the draw bead and the mating groove in the clamping ring.

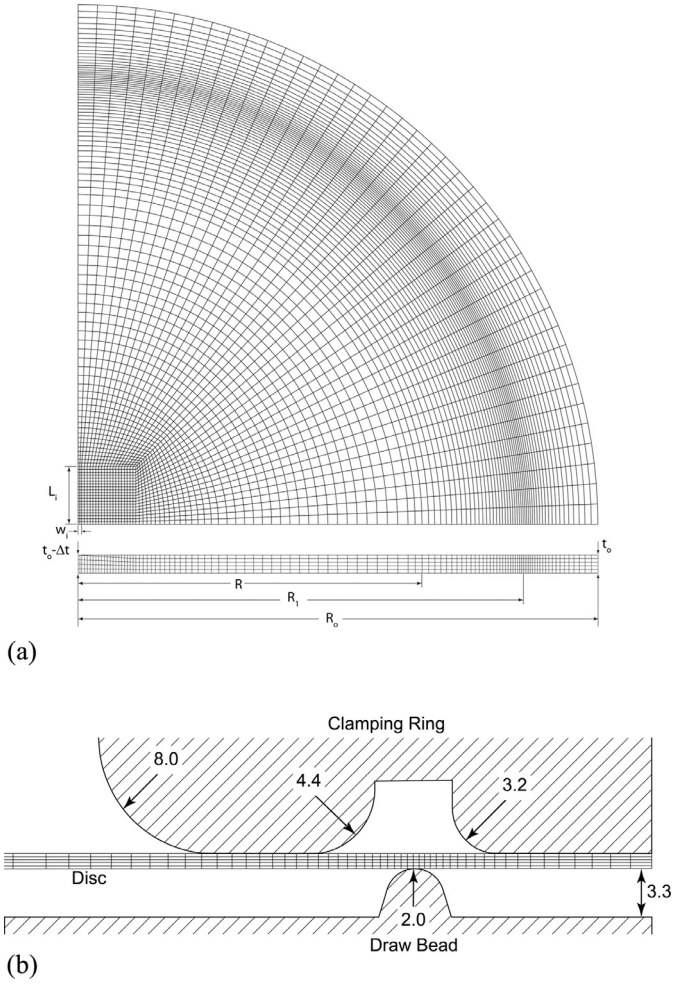

Fig. 10. (a) One quarter of the mesh adopted for our finite element model. (b) Close-up cross section of the model in the vicinity of the clamping ring and draw bead (indicated dimensions are in mm).

The disc is discretized with eight-node, reduced integration, linear solid elements (C3D8R). The base, including the draw bead, and the clamping ring are modeled as analytical rigid surfaces. Surface-to-surface frictional contact with finite sliding is adopted with Coulomb friction coefficient μ. An exponential "softened" contact pressure-overclosure relationship is used. The disc is discretized with a mesh with the following characteristics:

- 5 elements are used through the thickness.
- A 1-inch square section in the center of the disc has a more refined, nearly-isotropic mesh with 42×40 elements. A narrow ($2w_i \times 2L_i$) thickness imperfection with thickness ($t_o - \Delta t$) is introduced at the center of this area to facilitate localization.
- A nearly-uniform angular distribution of elements of 2.195° is used in the rest of the disc.
- The axial distribution of elements outside the central zone is as follows:
  - The circular zone, $r \leq 30.9$ mm, that surrounds the fine square mesh has 16 elements with a bias ratio of 2.
  - For $30.9 \leq r \leq 72.4$ mm there are 20 elements with a bias ratio of 1.2.
  - For $72.4 \leq r \leq 98.3$ mm there are 30 elements with a bias ratio of 4.
  - For $98.3 \leq r \leq 114.3$ mm there are 20 elements with a bias ratio of 4.

The initial cavity between the flat disc and the base is enclosed with 25,172 four-node fluid elements F3D4.

The disc is first clamped in place in a manner similar to that followed in the experiment. The base is fixed in space and the clamping ring is incrementally displaced downward while keeping the volume of fluid in the cavity constant. In the process a narrow ring of the disc engages the draw bead and the mating groove eventually "locking" the disc in place. Concurrently, the pressure in the cavity increases causing a small vertical displacement to the free section of the disc. When the clamping ring reaches the desired position it is fixed in space for the remainder of the simulation. Subsequently the model is pressurized by incrementally prescribing the flux of fluid into the cavity (volume-controlled pressurization).

4.1. Numerical simulation of the bulge test

The main characteristics of the solution are illustrated through the results of a simulation that uses the calibrated Yld04-3D constitutive model. Fig. 11a shows the calculated pressure-height ($P-h/R$) response. The model has no imperfection and a Coulomb coefficient of 0.4 is adopted. The calculated response tracks that of the experimental very closely (see Fig. 12) from the beginning to the end, and they are not included in this figure for clarity. A pressure maximum develops at 64.35 bar (933.05 psi), which compares with 64.26 bar (932.8 psi) recorded in the experiment. The analysis does not employ a failure criterion so the response is followed further than the experiment well past the pressure maximum. The evolution of the bulge profile is illustrated in Fig. 11b that shows the complete shape of a meridian at the pressure and height values marked with numbered bullets on the response in Fig. 11a (r = radial distance measured from the bulge center). Profile ⑦ corresponds to the pressure maximum. As in the experiments, the bulge profiles exhibit a progressive increase in curvature with height and a reduction of the rate of increase as the bulge height increases. Furthermore, as in the experiment, the shape of the bulge remains continuous past the pressure maximum and the apex maintains its nearly circular shape.

Fig. 11c shows the equivalent plastic strain (e_e^P) that develops in the same ten configurations, with profile ⑦ once more corresponding to the pressure maximum. In contrast to the bulge profiles, the strain profiles exhibit an increasingly tighter radius around the apex, which becomes significantly more pronounced after the pressure maximum. Thus in profiles ⑧-⑩, the zone around the apex becomes increasingly more conical indicating an acceleration of wall thinning. Simultaneously, the strain decreases nearly linearly with r moving away from the apex. These features are once again very similar to those of the experimental profiles in Fig. 3c. Fig. 11d compares the strain at the apex with that developed at $r=0.65R$. At lower values of bulge height the two strains grow at a similar rate gradually diverging. For $h > 0.4R$ when the pressure–height response starts to become nonlinear, the strains continue to grow at both locations but the trajectories increasingly diverge. Beyond the limit load (marked with solid bullets) the rate of growth of strain at the outer location where the bulge profile is becoming straighter, starts to decrease. By contrast, the strain at the apex grows at an even faster rate. This divergence in the rate of growth of strains is reminiscent of diffuse localized deformation such as a neck in a tensile test. However, in the present problem the pre-limit load stresses and deformations at the two locations are different.

The simulation of the bulge test was repeated using the Hosford (H8) and von Mises (vM) yield functions together with the corresponding stress–strain responses (Fig. 8). The calculated pressure-bulge height responses are compared in Fig. 12a to the experimental response (drawn with dashed line). On the scale of this plot, all three calculated responses track the experimental results very well. A small difference from the experiment observed below a pressure of about 7 bar (100 psi) is due to the fact that the deformation was not continuously monitored during the clamping process. To accentuate the small differences between the

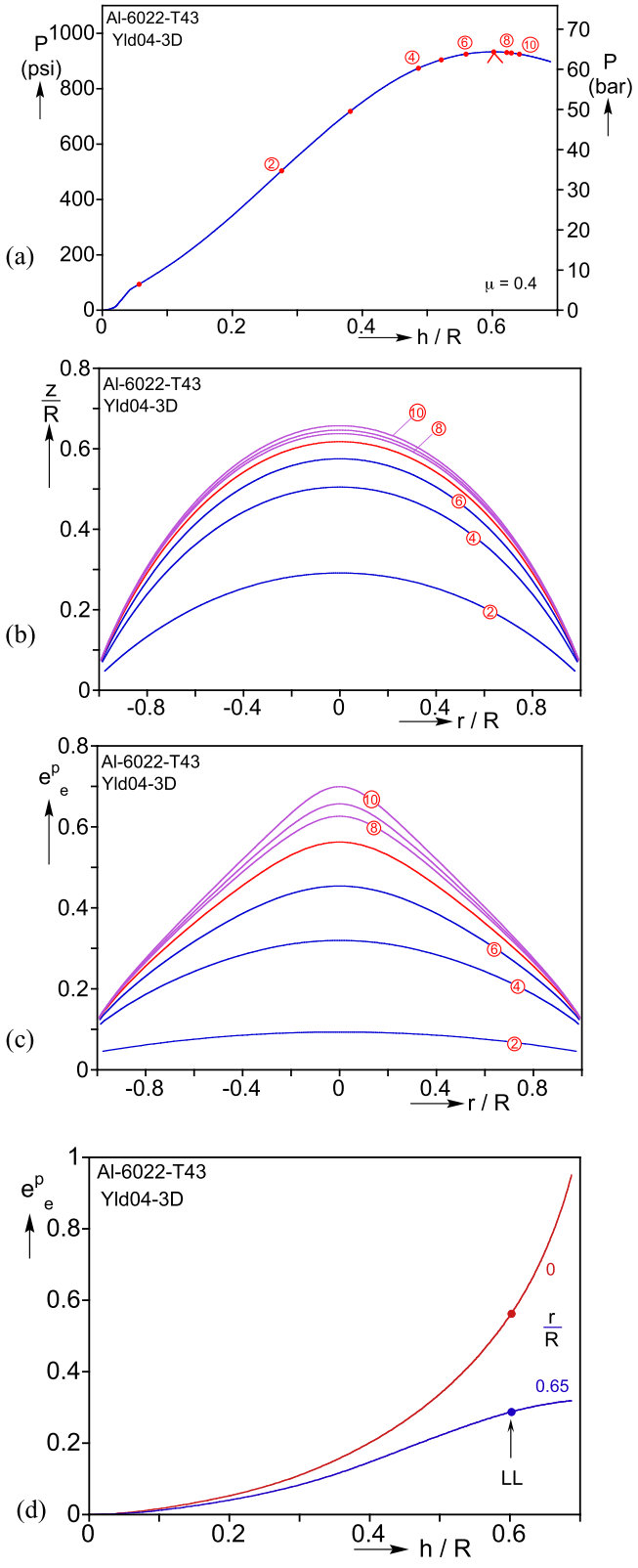

Fig. 11. Evolution of deformation in finite element simulation (analog to Fig. 3). (a) Pressure versus height response, (b) deformed surface profiles, and (c) corresponding equivalent strain profiles. (d) Evolution of equivalent plastic strain at the apex ($r=0$) and at a point a radial distance of $0.65R$ from the apex (location of pressure maximum denoted by LL).

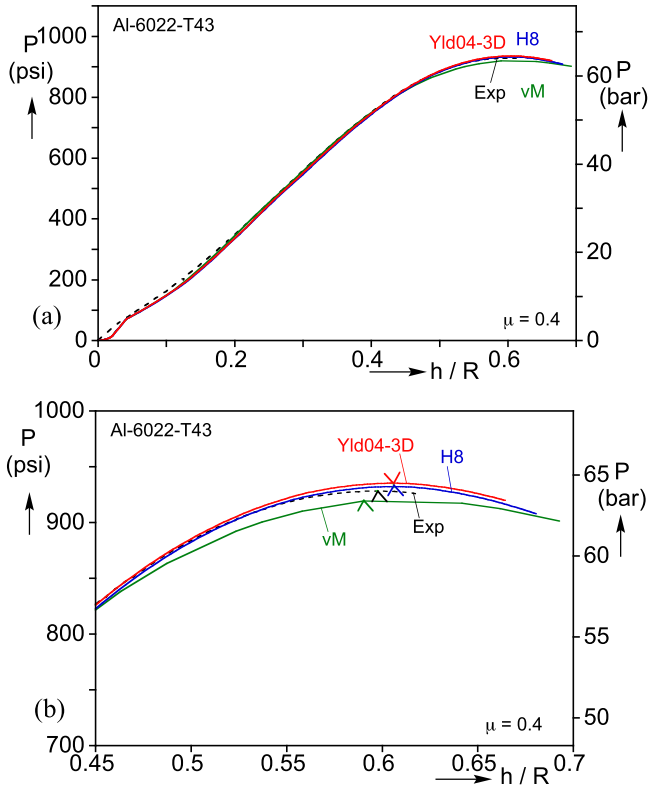

Fig. 12. (a) Predicted pressure versus height responses using three different constitutive models compared to the experimental response and (b) close-up view around the pressure maxima.

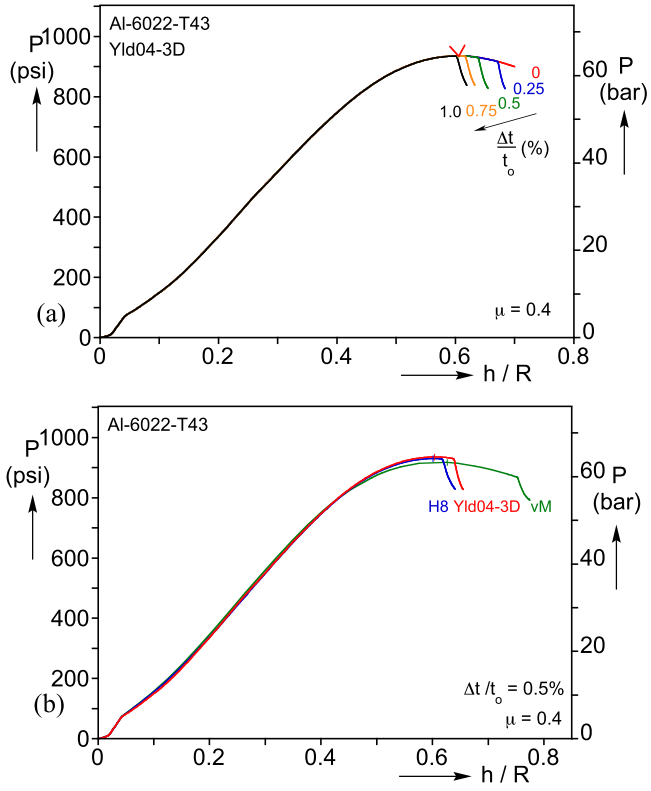

Fig. 13. (a) Effect of imperfection magnitude on predicted pressure versus height response. (b) Comparison of pressure-height responses for $\Delta t/t_o = 0.5\%$ using the vM, H8, and Yld04-3D models.

four responses around the pressure maxima, they are re-plotted in truncated scales of pressure and height in Fig. 12b. The pressure maximum of each response is now identified with a caret (^). As mentioned above, the Yld04-3D response nearly matches that of the experiment in all respects including the level of the pressure maximum. The H8 response is nearly identical to the Yld04-3D response, while the vM model's response traces a slightly lower pressure and pressure maximum. In addition, the strains at the three pressure maxima are in the neighborhood of 0.56 reported for Yld04-3D earlier. This close agreement between the three constitutive models indicates that the anisotropy present in this aluminum alloy sheet does not affect this particular problem with its nearly axisymmetric deformation. Apparently, neither do the differences between the shapes of the non-quadratic and quadratic yield surfaces. It is worth emphasizing, however, that the yield function and anisotropy can play a larger role in sheet metal forming applications with different stress-states.

In the simulations thus far the initial geometry of the model was perfect and the bulges remained free of localized wall thinning well past the pressure maxima that developed. To test the sensitivity of the solution to imperfections we introduce a narrow, linear thickness imperfection in the center of the disc along the transverse direction (y') with dimensions $(2L_i, 2w_i) = (0.33R, 1.27t_o)$ and wall thickness reduction of Δt. Fig. 13a shows the pressure–height response of the perfect case together with the responses of four discs assigned imperfection amplitudes of: $\Delta t/t_o = \{0.25,\ 0.5,\ 0.75,\ 1.0\}\%$. The responses are indistinguishable from that of the perfect case until the point when the deformation in the imperfection accelerates, which coincides with a sharp drop in pressure (see Fig. 17 of [12] for a detailed depiction of the evolution of this deformation). This type of event is expected to cause rupture so the point of downturn in the response can be considered to be the critical state of each solution. As the imperfection increases, the critical point occurs at increasingly smaller values of bulge height. Overall, this behavior indicates that due to the nearly equibiaxial state of stress at the apex, the structure is not very imperfection sensitive. It is worth noting that in view of the observed tendency of accelerated wall thinning at the apex of the bulge after the pressure maximum, we have also considered wall-thinning imperfections of circular shape at the center of the disc. The solution was found to be even less sensitive to this type of imperfection.

The effect of a linear thickness imperfection on the response calculated using the two isotropic models vM and H8 is also examined. Fig. 13b compares the pressure–height responses of the two models with the corresponding one from Yld04-3D for thickness imperfections of 0.5%. The imperfection has essentially no influence on the overall response of the structure so the three responses are nearly identical to those shown in Fig. 12a. However, the state of stress inside and in the neighborhood of the imperfection is altered, which leads to differences in the onset of localization predicted by the three constitutive models. The H8 model localizes earlier than Yld04-3D whereas for vM localization takes place late in the post-limit load regime. Furthermore, the strain at the onset of localization is also different, achieving a value of 0.66 for Yld04-3D, 0.61 for H8 and larger than 1.0 for vM. Clearly, the difference between the H8 and Yld04-3D is mainly caused by anisotropy, while the difference between H8 and vM results from the different exponent of the two yield functions. This confirms that both of these constitutive issues influence sheet metal forming of Al alloys.

The solutions presented above were generated with a Coulomb friction coefficient $\mu = 0.4$. In [12] we pointed out that slipping over the draw bead can affect the calculated response. The amount of slipping is governed by the extent of mechanical clamping and by friction. In the facility shown in Fig. 1, the imposed displacement of the clamping ring was chosen to be as large as possible without causing failure of the disc at the draw bead. This process does not preclude some small amount of slipping at the draw bead. Consequently it is important that the effect of slipping on the response be evaluated. To this end, the bulge test simulation is repeated using the Yld04-3D constitutive model and Coulomb friction coefficients of 0.3, 0.4 and 0.5 and a thickness imper-

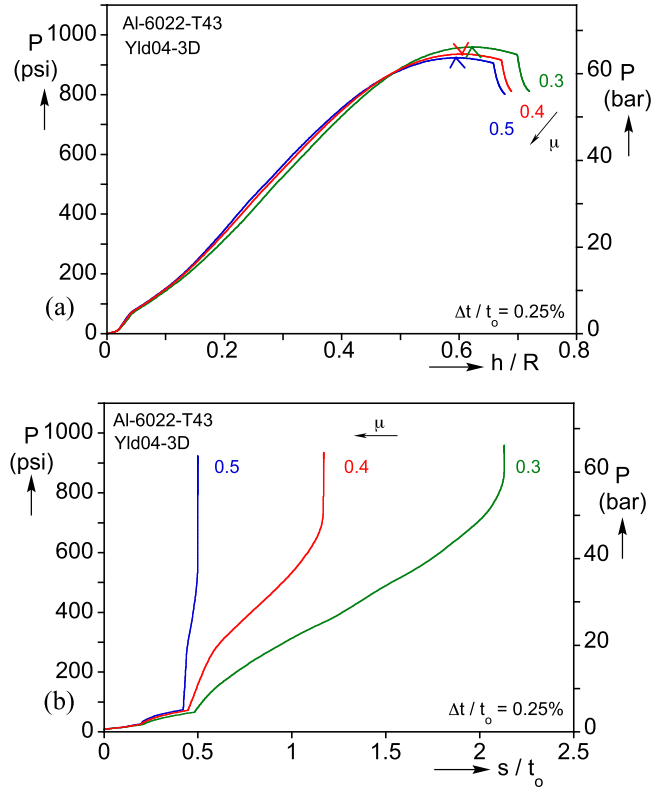

Fig. 14. Effect of friction coefficient on (a) predicted pressure versus height response, and (b) magnitude of radial displacement of the disc boundary.

fection of $\Delta t/t_o = 0.25\%$. The calculated pressure-bulge height responses are shown in Fig. 14a. The magnitude of inward sliding of the outer edge, s, normalized by t_o, is plotted against the pressure in Fig. 14b. Clearly, increase in friction lowers the pressure maximum and causes it to occur at a smaller bulge height. The amount of sliding exhibits an initial transient caused by the clamping process, which is nearly identical for the three values of μ. Subsequently, s increases monotonically but saturates at higher pressure levels. For $\mu = 0.3$ the total amount of sliding is greater than $2t_o$, whereas for $\mu = 0.5$ the disc is essentially fixed in place after the initial transient.

The extra feed of material into the bulging domain allowed by sliding is responsible for the larger height reached for lower μ values, and for the increase in P_{max} observed in Fig. 14a and quantified in the Table below. At the same time however, it is noteworthy that the strain achieved at the pressure maximum decreases as the pressure and corresponding bulge height increase, as the values reported in the same Table indicate. (This result can also be demonstrated analytically using an extension of Hill's analysis of the critical strain–Appendix B.)

μ	0.3	0.4	0.5
P_{max}	958.5	935.2	922.6
e_e^p	0.53	0.56	0.57

Since most bulge testing facilities used in materials labs are relatively compliant, the bulge is expected to fail at the pressure maximum or soon thereafter. Clearly then, it can be concluded that better clamping can have the beneficial effect of increased strain measured in a bulge experiment. In the present simulations, the response for $\mu = 0.4$ was closest to the experimental response so this friction coefficient was adopted in the parametric study performed.

It should be mentioned that in the simulations presented sliding is axisymmetric and uniform. In practice, non-uniform, asymmetric slipping may take place as illustrated by the failed specimen shown in Appendix C from a previous study. Slipping can influence the state of stress and strain at the apex and, by extension, the extracted stress–strain response. In general then, every effort should be made to reduce slipping in bulge tests, as recommended in ISO 2014 [9].

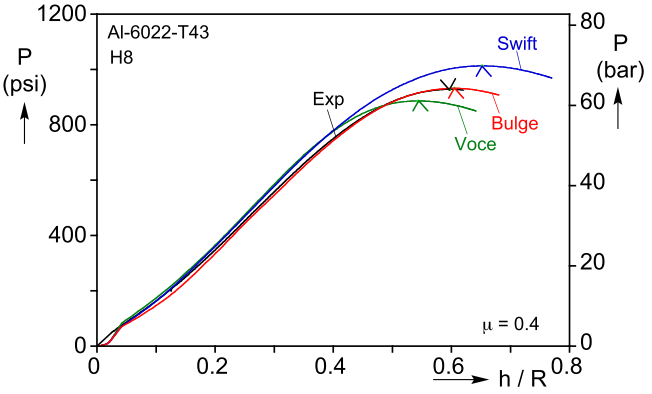

Fig. 15. Predicted pressure versus height response using three different stress–strain curves shown in Fig. 9. The measured experimental response is included.

Finally, to assess the effect of the stress–strain response adopted on the numerical simulation of the bulge test, the FE model was used to calculate the bulge response using the Swift and Voce extrapolations of the uniaxial response shown in Fig. 9. Fig. 15 compares the pressure-height responses calculated using these two stress–strain responses with that produced using the stress–strain response extracted from the bulge test. Here the H8 constitutive model is adopted for all three cases. As pointed out in the discussion of Fig. 12, the H8 prediction using the stress–strain response extracted from the bulge test is very close to the experimental one. As expected, the response produced by the Swift extrapolation overestimates the experimental response and the Voce underestimates it, pointing to the inadequacies of such extrapolations.

5. Summary and conclusions

The hydraulic bulge test enables direct measurement of the material stress–strain response of sheet metal to strains far larger than other tests. The nearly equibiaxial stress state and continuous reduction of the local radius at the apex delay wall thinning and the associated limit pressure instability. The relatively recent development of full-field optical methods like digital image correlation enables continuous measurement of deformation and has generated renewed interest in the bulge test. This paper reports the extraction of the stress–strain response of an anisotropic, ductile aluminum alloy using a combination of bulge experiments and analyses. Bulge tests on 1.20 mm Al-6022-T43 sheet were conducted in a custom facility with a 150 mm aperture, with continuous monitoring of deformation using DIC. The ductility of this alloy enabled it to deform well past a pressure maximum reaching a strain of 0.66 before the bulge ruptured. By comparison, the strain at the load maximum in a uniaxial tension test was 0.20, demonstrating the advantages of the bulge test. After the pressure maximum, the strain profile took on an increasingly more conical shape, and was accompanied by an acceleration of wall thinning around the apex. Although this phenomenon has been reported in a few past experiments, this is the first time it has been captured to such a significant detail due to the additional capability afforded by DIC.

The material was found to have a unique anisotropy that was modeled via the anisotropic Barlat et al. Yld04-3D [22] yield function. The rather elaborate calibration of this constitutive model was performed through a set of independent experiments. The results are new and useful to researchers and practitioners working with this alloy. A membrane stress state is assumed to exist at the apex but in view of the anisotropy, neither an equibiaxial state of stress or strain was assumed. The stress–strain response is extracted incrementally using the measured strains

and radii of curvature in the two principal directions together with the constitutive and equilibrium equations. This added an iterative step to the stress–strain extraction process, which is avoided if the anisotropy is known a priori. The stress–strain response of the material was also established using the von Mises and the Hosford yield functions.

A finite element model was subsequently used to simulate the bulge test. The model discretizes the disc with solid elements, allows for the possibility of slipping over the draw bead, and incorporates the calibrated anisotropic yield function and the extracted stress–strain response. The calculated results reproduce the experimental measurements very closely, including the pressure-height response, the pressure maximum, and the deformed strain profile and its evolution into a more conical shape after the pressure maximum. This is the first time the latter has been reproduced numerically.

Additional findings and conclusions from the study follow in brief.

- The measured radii of curvature in the rolling and transverse direction were essentially the same, but because of the anisotropy the strains were different and so were the calculated stresses. Despite this, the stress–strain responses extracted using vM and H8 tracked closely the one from the anisotropic model. Furthermore, FE simulations of the bulge test using these constitutive models reproduced the experimental results also. These results indicate that the particular anisotropy of the analyzed sheet does not affect the bulge test in any significant manner. However, the anisotropy is expected to play a larger role in problems with different stress states than that of the bulge test.
- Slipping of the clamped disc at the draw bead affects the response, causes a decrease in the strain at the pressure maximum, and must be accounted for in the modeling. Asymmetric slipping, on the other hand, can result in additional complexity in the extraction of the stress–strain response (see approach in [12]). Thus every effort should be made to minimize slipping in bulge tests. In the reported experiments, improved clamping made the proposed extraction process simpler, and therefore more accessible to the sheet metal forming researcher.
- The sensitivity of the bulge test to small thinning imperfections at the apex was examined and its effect was found to be mild. However, the change of the state of stress in the neighborhood of the imperfection changes the onset of localization predicted by Yld04-3D, vM, and H8. This reinforces the need for a suitably calibrated anisotropic yield function.
- Extrapolations of the uniaxial stress–strain response based on the commonly used Voce and Swift fits respectively underestimated and overestimated the actual response significantly. Adoption of these extrapolations in the FE simulation of the bulge test resulted in significant deviations from the measured results. The reported differences are of paramount importance in forming simulations, and especially in calculations of FLDs, as well as in other calculations involving large deformations. A fit of the uniaxial response that combines the Swift and Voce expressions produces an extrapolation that is much closer to the measured response, but overestimates the tangent modulus at higher strain values.

Acknowledgments

The work reported was conducted with financial support from Sandia National Laboratories and the National Science Foundation through grant CMMI-1663269. This support is acknowledged with thanks. We also thank Edmund Chu of Alcoa for providing the sheet metal used in the experiments and for constructive comments.

Appendix A: Results of anisotropy experiments

Results from three sets of experiments conducted on Al-6022-T43 sheets for the purpose of calibrating the Yld04-3D anisotropic yield function are summarized here. Fig. A1 shows the complete nominal stress–strain response measured in the rolling direction. Fig. A2 shows the true stress-logarithmic strain responses and axial-transverse strain responses from the seven tensile tests performed at 15° intervals between the rolling and transverse directions of the Al-6022-T43 sheet. Fig. A3 shows the test specimen used in the plane-strain tests and the three ax-

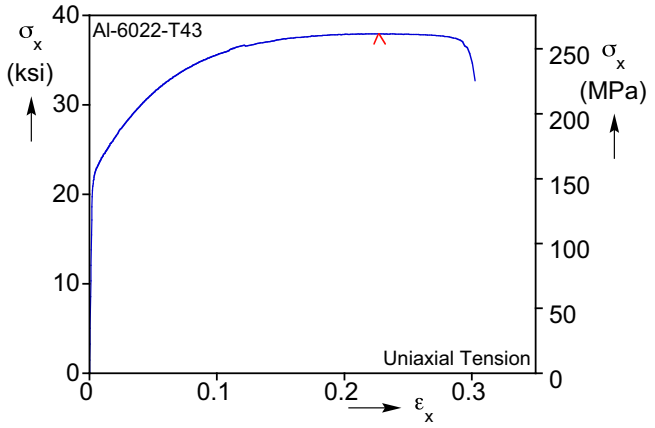

Fig. A1. Nominal uniaxial stress–strain response in the rolling direction.

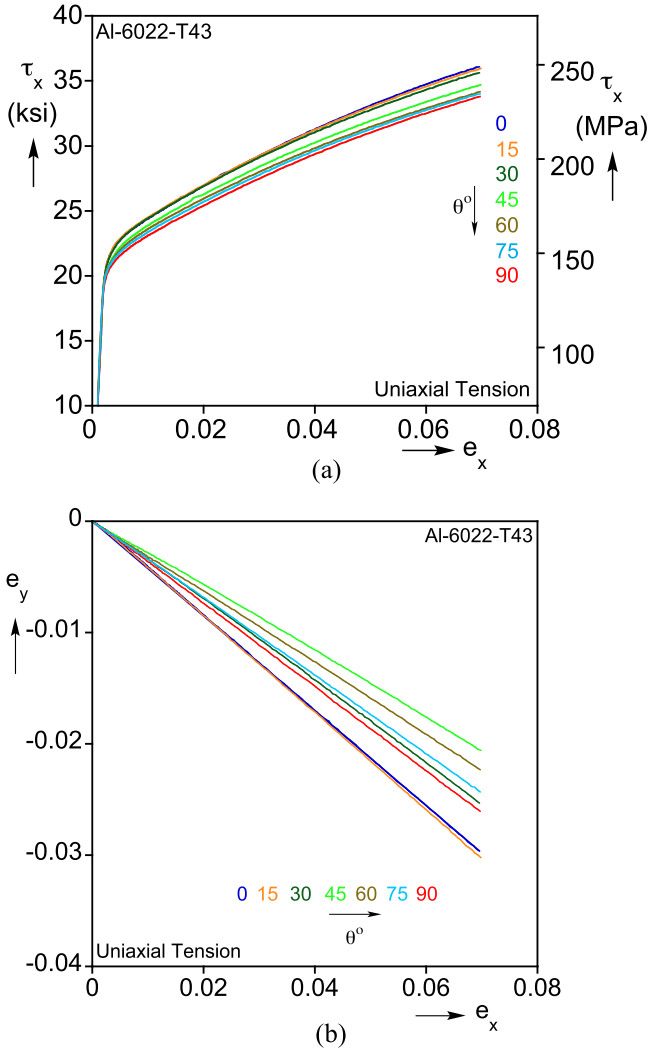

Fig. A2. (a) True stress–strain responses of the seven uniaxial tension tests used for calibrating the Yld04-3D constitutive model. (b) Corresponding transverse versus axial strain paths.

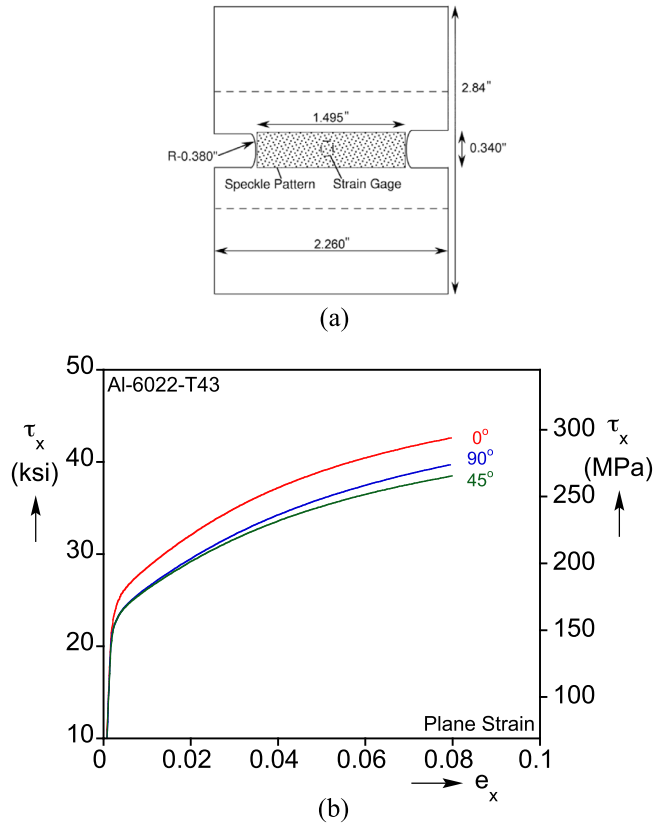

Fig. A3. (a) Drawing of the plane-strain tension specimen used for calibration. (b) Responses from the three plane-strain tests.

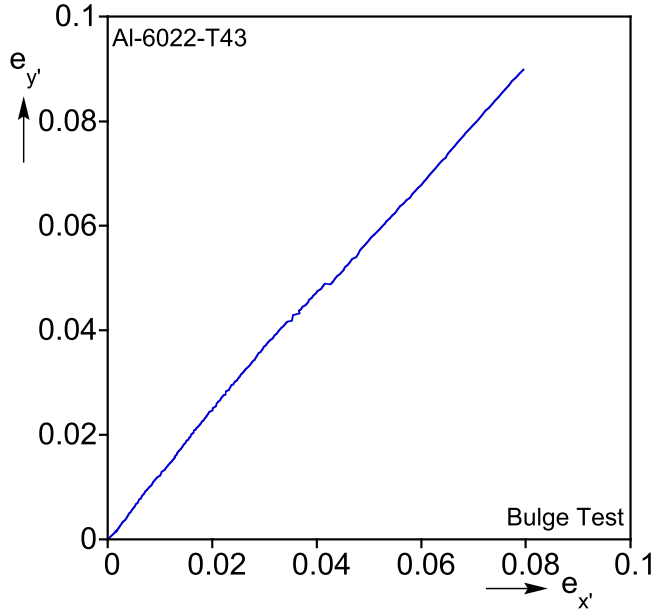

Fig. A4. Transverse versus rolling-direction strain path measured in the bulge test and used to calibrate the Yld04-3D constitutive model.

ial stress–strain responses measured in the middle of the test section. Fig. A4 shows plots of the rolling direction strain versus and transverse direction strain in the early stages of the bulge test.

Appendix B: Hill's Bulge analysis [1950]

Hill's approximate but insightful analysis of a bulge test [16] is based on the assumption that it deforms into a spherical shape (see also [15] earlier approximate solution). It leads to the following relationship between the through thickness strain at the apex, e_t, the height of the bulge h and its polar radius ρ:

$$-e_t = ln\left(\frac{t_o}{t}\right) = 2ln\left(1+\frac{h^2}{R^2}\right), \tag{B1a}$$

and

$$\frac{\rho}{R} = \left(1+\frac{h^2}{R^2}\right)/\frac{2h}{R}. \tag{B1b}$$

The equibiaxial state of stress at the apex relates the stress, τ, to the instantaneous values of the variables through

$$\frac{2\tau}{\rho} = \frac{P}{t} \tag{B2}$$

$$\text{At } P_{\max},\ \frac{d\tau}{\tau}+\frac{dt}{t}-\frac{d\rho}{\rho}=0 \tag{B3}$$

For von Mises yielding,

$$\tau_e = \tau \text{ and } de_e = 2de = -\frac{dt}{t}. \tag{B4}$$

$$\text{Then (B3)} \rightarrow \frac{1}{\tau_e}\frac{d\tau_e}{de_e} = 1+\frac{1}{\rho}\frac{d\rho}{de_e} \tag{B5}$$

$$\text{Using (B1) in (B5)}\ \frac{1}{\tau_e}\frac{d\tau_e}{de_e} = \frac{3}{2}-\frac{\rho}{2h} \tag{B6}$$

Expanding ρ/h in terms of e_e, leads to the following approximate expression for the critical state

$$\frac{1}{\tau_e}\frac{d\tau_e}{de_e} \approx \frac{11}{8}-\frac{1}{2e_e}. \tag{B7}$$

Using the material response extracted from the bulge test and the von Mises yield function in (B7) results in a critical strain of 0.44, which compares with 0.528 measured in the experiment. Since the stress–strain response extracted from the bulge using the von Mises yield function is very similar to the one based on Yld04-3D, the corresponding instability strain resulting from (B7) is very close to 0.44. This difference between the values produced by the complete bulge numerical analysis and Hill's closed form expression is of course caused by the approximate nature of that solution.

For completeness, the Swift and Voce extrapolations of the measured uniaxial response of Al-6022-T43 were implemented in (B7) in conjunction with the von Mises yield criterion. The calculated critical strains are 0.54 for Swift and 0.40 for Voce. The critical strains are marked on the corresponding stress–strain responses with sold bullets in Fig. 9.

Appendix C: Effect of slipping

Fig. C1 shows a failed bulge test specimen that experienced slipping at the draw bead during the initial development of our bulge test facility. The slipping is unsymmetric and is much more pronounced at the lower end where wrinkles developed.

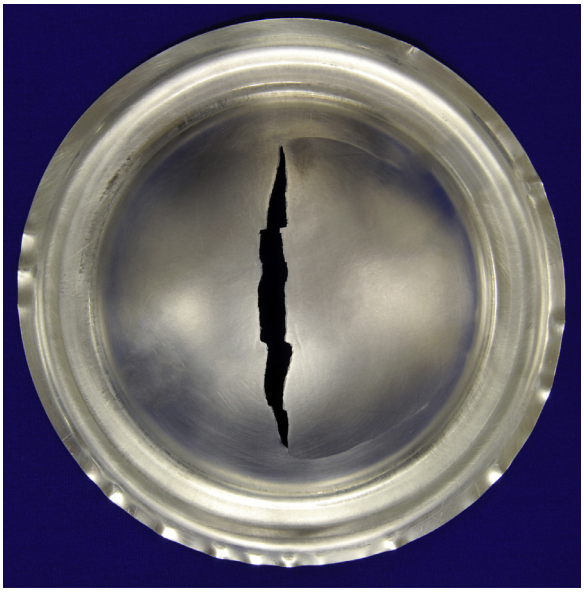

Fig. C1. A bulge test specimen that experienced asymmetric slipping.

References

[1] Brown WF, Sachs G. Strength and failure characteristics of thin circular membranes. Trans ASME 1948;70:241–51.
[2] Mellor PB. Stretch forming under fluid pressure. J Mech Phys Solids 1956;5:41–56.
[3] Ranta-Eskola AJ. Use of the hydraulic bulge test in biaxial tensile testing. Int J Mech Sci 1979;21:457–65.
[4] Young RF, Bird JE, Duncan JL. An automated hydraulic bulge tester. J Appl Metal Working 1981;2:11–18.
[5] Santos AD, Teixeira P, Barata da Rocha A, Barlat F. On the determination of flow stress using bulge test and mechanical measurements. In: Proc. Tenth International Conf. NUMIFORM 2010; 2010. p. 845–52. June 13-17.
[6] Amaral R, Santos AD, Lopes AB. Mechanical properties determination of dual-phase steels using uniaxial tensile and hydraulic bulge test. Ciencia Technol dos Mater 2017;27:e239–2343.
[7] Vucetic M, Bouguecha A, Peshekhodov I, Gotze T, Huinink T, Friebe H, Moller T, Behrens B-A. Numerical validation of analytical biaxial true stress-true strain curves from the bulge test. In: Proc. Eighth Int'l Conf. NUMISHEET 2011; 2011. p. 107–14. August 21-26.
[8] Lăzărescu L, Nicodim I, Ciobanu I, Comşa DS, Banabic D. Determination of material parameters of sheet metals using the hydraulic bulge test. Acta Metall Slovaca 2013;19:4–12.
[9] DIN EN ISO 16808:2014(E). Metallic materials–sheet and strip—Determination of the biaxial stress-strain curve by means of a bulge test with optical measuring systems (2014).
[10] Mulder J, Vegter H, Aretz H, Keller S, van den Boogaard AH. Accurate determination of flow curves using the bulge test with optical measuring systems. J Mater Process Technol 2015;226:169–87.
[11] Aretz H, Keller S. On the non-balanced biaxial stress state in bulge-testing. Steel Res Int 2011:738–43 Special Edition.
[12] Chen K, Scales M, Kyriakides S, Corona E. Effects of anisotropy on material hardening and burst in the bulge test. Int J Solids Struct 2016;82:7–84.
[13] Suttner S, Merkelein M. Experimental and numerical investigation of a strain rate controlled hydraulic bulge test of sheet metal. J Mater Process Technol 2016;235:121–33.
[14] Reis LC, Parates PA, Oliveira MC, Santos AD, Fernandes JV. Anisotropy and plastic flow in a circular bulge test. Int J Mech Sci 2017;128-129:70–93.
[15] Gleyzal A. Plastic deformation of a circular diaphragm under pressure. Trans ASME 1948;70:288–96.
[16] Hill R. A theory of plastic bulging of a metal diaphragm by lateral pressure. Philos Mag 1950;7:1133–42.
[17] Chakrabarty J, Alexander JM. Hydrostatic bulging of circular diaphragms. J Strain Anal Eng 1970;5:155–61.
[18] Atkinson M. Accurate determination of biaxial stress-strains relationships from hydraulic bulging tests of sheet metals. Int J Mech Sci 1997;39:761–9.
[19] Banabic D, Balan T, Comsa DS. Closed-form solution for bulging through elliptical dies. J Mater Process Technol 2001;115:83–6.
[20] Rees DWA. Plastic flow in the elliptical bulge test. Int J Mech Sci 1995;37:373–89.
[21] Kamat RG, Butler JF, Murtha SJ, Bovard FS. Alloy 6022-T4E29 for automotive sheet applications. Mater Sci Forum 2002;396-402:1591–6.
[22] Barlat F, Aretz H, Yoon JW, Karabin ME, Brem JC, Dick RE. Linear transformation-based anisotropic yield functions. Int J Plast 2005;21:1009–39.
[23] Yanaga D, Kuwabara T, Uema N, Asano M. Material modeling of 6000 series aluminum alloy sheets with different density cube textures and effect on the accuracy of finite element simulation. Int J Solids Struct 2012;49:3488–95.
[24] *ARAMIS User Manual-Software*. GOM Optical Measuring Techniques, 23 May 2011. PDF
[25] Hosford WF. A generalized isotropic yield criterion. ASME J Appl Mech 1972;39:607–9.
[26] Giagmouris T, Kyriakides S, Korkolis YP, Lee L-H. On the localization and failure in aluminum shells due to crushing induced bending and tension. Int J Solids Struct 2010;47:2680–92.
[27] Tardif N, Kyriakides S. Determination of anisotropy and material hardening for aluminum sheet metal. Int J Solids Struct 2012;49:3496–506.
[28] Korkolis YP, Kyriakides S. Inflation and burst of anisotropic tubes for hydroforming applications. Int J Plast 2008;24:509–43.
[29] Korkolis YP, Kyriakides S. Inflation and burst of aluminum tubes part II: An advanced yield function including deformation-induced anisotropy. Int J Plast 2008;24:1625–37.
[30] Korkolis YP, Kyriakides S. Path-dependent failure of inflated aluminum tubes. Int J Plast 2009;25:2059–80.
[31] Korkolis YP, Kyriakides S, Giagmouris T, Lee L-H. Constitutive modeling and rupture predictions of Al-6061-T6 tubes under biaxial loading paths. ASME J Appl Mech 2010;77(5):1–5 064501.
[32] Dunand M, Maertens AP, Luo M, Mohr D. Experiments and modeling of anisotropic aluminum extrusions under multi-axial loading–Part I: plasticity. Int J Plast 2012;36:34–49.
[33] Yoon JW, Barlat F, Dick RE, Karabin ME. Prediction of six or eight ears in a drawn cup based on a new anisotropic yield function. Int J Plast 2006;22:174–93.
[34] Yoon, J.W. (2009, 2011). Personal communications.
[35] Tian H, Brownell B, Baral M, Korkolis YP. Earing in cup-drawing of anisotropic Al-6022-T4 sheets. Int J Mater Forming 2017;10:329–43.
[36] Swift HW. Plastic instability under plane stress. J Mech Phys Solids 1952;1:1–18.
[37] Voce E. The relationship between stress and strain for homogeneous deformation. J Inst Met 1948;74:537–62.
[38] Reis LC, Parates PA, Oliveira MC, Santos AD, Fernandes JV. Inverse identification of the Swift law parameters using the bulge test. Int J Mater Form 2017;10:493–513.
[39] Sung JH, Kim JH, Wagoner RH. A plastic constitutive equation incorporating strain, strain-rate, and temperature. Int J Plast 2010;26:1746–71.